

# Image quality assessment of LaBr<sub>3</sub>-based whole-body 3D PET scanners: a Monte Carlo evaluation

To cite this article: S Surti *et al* 2004 *Phys. Med. Biol.* **49** 4593

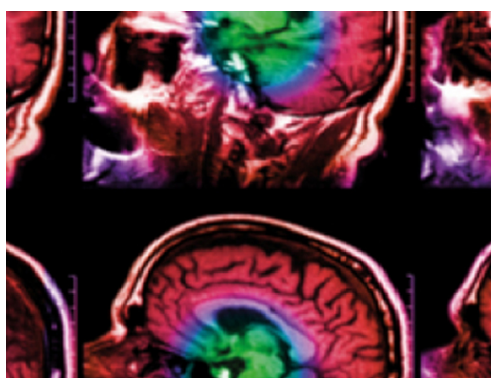
View the [article online](#) for updates and enhancements.

## Related content

- [A count-rate model for PET scanners using pixelated Anger-logic detectors with different scintillators](#)  
S Surti and J S Karp
- [The imaging performance of a LaBr<sub>3</sub>-based PET scanner](#)  
M E Daube-Witherspoon, S Surti, A Perkins *et al.*
- [Impact of detector design on imaging performance of a long axial field-of-view, whole-body PET scanner](#)  
S Surti and J S Karp

## Recent citations

- [Radiation visualization in radiation oncology](#)  
D. Dzhuzha
- [State of the art in total body PET](#)  
Stefaan Vandenberghe *et al*
- [Impact of event positioning algorithm on performance of a whole-body PET scanner using one-to-one coupled detectors](#)  
S Surti and J S Karp



**IPEM | IOP**

Series in Physics and Engineering in Medicine and Biology

Your publishing choice in medical physics,  
biomedical engineering and related subjects.

Start exploring the collection—download the  
first chapter of every title for free.

# Image quality assessment of LaBr<sub>3</sub>-based whole-body 3D PET scanners: a Monte Carlo evaluation

S Surti<sup>1</sup>, J S Karp<sup>1</sup> and G Muehllehner<sup>2</sup>

<sup>1</sup> Department of Radiology, University of Pennsylvania, 3400 Spruce Street, Philadelphia, PA 19104, USA

<sup>2</sup> Philips Medical Systems, Philadelphia, PA 19104, USA

Received 19 March 2004

Published 20 September 2004

Online at [stacks.iop.org/PMB/49/4593](http://stacks.iop.org/PMB/49/4593)

doi:10.1088/0031-9155/49/19/010

## Abstract

The main thrust for this work is the investigation and design of a whole-body PET scanner based on new lanthanum bromide scintillators. We use Monte Carlo simulations to generate data for a 3D PET scanner based on LaBr<sub>3</sub> detectors, and to assess the count-rate capability and the reconstructed image quality of phantoms with hot and cold spheres using contrast and noise parameters. Previously we have shown that LaBr<sub>3</sub> has very high light output, excellent energy resolution and fast timing properties which can lead to the design of a time-of-flight (TOF) whole-body PET camera. The data presented here illustrate the performance of LaBr<sub>3</sub> without the additional benefit of TOF information, although our intention is to develop a scanner with TOF measurement capability. The only drawbacks of LaBr<sub>3</sub> are the lower stopping power and photo-fraction which affect both sensitivity and spatial resolution. However, in 3D PET imaging where energy resolution is very important for reducing scattered coincidences in the reconstructed image, the image quality attained in a non-TOF LaBr<sub>3</sub> scanner can potentially equal or surpass that achieved with other high sensitivity scanners. Our results show that there is a gain in NEC arising from the reduced scatter and random fractions in a LaBr<sub>3</sub> scanner. The reconstructed image resolution is slightly worse than a high-Z scintillator, but at increased count-rates, reduced pulse pileup leads to an image resolution similar to that of LSO. Image quality simulations predict reduced contrast for small hot spheres compared to an LSO scanner, but improved noise characteristics at similar clinical activity levels.

## 1. Introduction

There has been considerable research and development of inorganic scintillators for PET imaging over the past several decades (van Eijk 2002) and the search for the ideal scintillator is intensifying. The ideal scintillator has high light output, high stopping power and fast

**Table 1.** Scintillation properties of PET scintillators. Data are collected from van Eijk (2002) and Moszyński *et al* (1998), although the values of relative light output and energy resolution for LaBr<sub>3</sub> represent an average over different crystal geometries as measured in our laboratory.

Scintillator	$\tau$ (ns)	$\mu$ (cm <sup>-1</sup> )	$\frac{\Delta E}{E}$ (%)	Relative light output (%)
NaI(Tl)	230	0.35	6.6	100
BGO	300	0.95	10.2	15
GSO	60	0.70	8.5	25
LSO	40	0.86	10.0	75
LaBr <sub>3</sub> (5% Ce)	25	0.47	3.7	175

decay time. Recently we have become interested in the development of a new lanthanum bromide (LaBr<sub>3</sub>) scintillator (Surti *et al* 2003b, Kuhn *et al* 2004) that has been developed by van Loef at Delft University (van Loef *et al* 2001), and also reported on by Shah *et al* (2002). The low melting point of the LaBr<sub>3</sub> scintillators (783 °C) suggests that in the long run this scintillator can be cost-effective. Table 1 summarizes some properties of LaBr<sub>3</sub> as well as other scintillators such as sodium iodide (NaI(Tl)), bismuth germanate (BGO), gadolinium orthosilicate (GSO) and lutetium orthosilicate (LSO) which are used in PET. As can be seen from this table, LaBr<sub>3</sub> is a very bright and fast scintillator. Its only drawback is the low stopping power ( $\mu$ ).

For clinical whole-body PET imaging, where a spatial resolution in the range of 4–6 mm is adequate for most investigations, there are primarily two scintillation detector designs in wide use. One is the standard NaI(Tl)-based Anger detector using a large NaI(Tl) scintillator coupled through a lightguide to an array of large photomultiplier tubes (PMTs) for signal readout and positioning (Anger 1958). The Anger detector has been successfully used in the design of hybrid PET/SPECT scanners, for example Nellemann *et al* (1995), as well as a dedicated whole-body PET scanner (C-PET) (Adam *et al* 2001). A recent variant on this design is the pixelated Anger-logic detector (Surti *et al* 2000) which uses an array of small pixelated crystals (not necessarily NaI(Tl)) optically coupled via a lightguide to a large array of PMTs. The advantage of the pixelated Anger-logic detector over the conventional Anger detector is the reduced light spread, and hence deadtime, achieved in the detector due to an optimized lightguide design. Pixelated Anger detectors using NaI(Tl) in a whole-body scanner design (Perkins *et al* 2003) and GSO for a whole-body (Surti and Karp 2004), brain (Karp *et al* 2003) and animal scanner designs (Surti *et al* 2003c) have been used by our group. The other primary detector is the block detector design (Casey and Nutt 1986) which typically uses a small array of crystals optically coupled through a lightguide to four relatively small PMTs, and which has been used in many BGO-based PET scanner designs, for example the GE Advance (Lewellen *et al* 1996) and the CTI HR<sup>+</sup> (Brix *et al* 1997). A variant of this design is the quadrant sharing block design (Wong *et al* 1995) which achieves similar spatial resolution as the conventional block detector but with larger PMTs. This detector design has been implemented in various versions of a variable diameter PET scanner (Uribe *et al* 1999) as well as commercial dedicated brain scanner, CTI HRRT (Wienhard *et al* 2002). Recent use of GSO and LSO scintillators in the current generation of whole-body scanners such as the GSO-based Philips Allegro (Surti and Karp 2004) and LSO-based CTI Accel (Erdi *et al* 2004) has focused on using either the pixelated Anger-logic detector (Allegro) or the block detector (Accel) to achieve good spatial resolution and high count-rate capability necessary to obtain good quality clinical whole-body images.

In this investigation, our aim is to predict the image quality performance of PET scanners based on a discrete Anger-logic detector (Surti *et al* 2000) using primarily LSO and LaBr<sub>3</sub> as the scintillator. The excellent timing resolution of LSO and LaBr<sub>3</sub> also leads to the

possibility of using time-of-flight information in achieving even better noise characteristics for clinical whole-body imaging (Moses and Derenzo 1999, Surti *et al* 2003b). Although we intend to develop a time-of-flight (TOF) capable detector for a PET scanner (Kuhn *et al* 2004), this paper does not address the additional benefit in performance that results from inclusion of TOF information in image reconstruction. However, these simulations form the basis for an investigation with TOF, as the timing information is already included in the list-mode data generated here. The TOF PET scanners developed in 1980s were based on caesium fluoride (CsF) (Allemand *et al* 1980, Mullani *et al* 1981) and barium fluoride (BaF<sub>2</sub>) (Ter-Pogossian *et al* 1981) which had inferior sensitivity and spatial resolution compared to the non-TOF BGO scintillator. The TOF measurement helped these scintillators to overcome the disadvantage with respect to BGO. Here we study the relative performance of LaBr<sub>3</sub> with respect to LSO. LaBr<sub>3</sub> has lower stopping power compared to LSO, just as CsF and BaF<sub>2</sub> have lower stopping power compared to BGO. The main difference is that now the whole-body PET scanners are designed for use in a fully 3D mode where the better energy resolution, faster decay and extremely high light output of LaBr<sub>3</sub> (30 times that of CsF and BaF<sub>2</sub>) can help overcome its disadvantages relative to LSO.

The goal of this study is three-fold: to predict the system NEC rates, calculate reconstructed image resolution and obtain reconstructed image quality phantom results to assess the impact of the scintillator properties. For the NEC rates, we study the impact of scintillator stopping power and scanner axial field-of-view on the system sensitivity. Additionally, the improved energy resolution allows the use of a narrow energy gate to reduce the scatter fraction (SF), and improved timing characteristics allow the use of a short coincidence timing window to reduce randoms. Also, since these scanner designs are based on Anger-logic detectors, we model pulse pileup and deadtime, and in particular calculate the degradation in SF as a function of count-rate while keeping the energy gates fixed. For spatial resolution, we reconstruct sinograms for a point source placed in the scanner to obtain reconstructed image resolution for a given scanner design. The image resolution is dependent on the crystal stopping power and Compton scatter cross-talk within crystals, as well as light output of the scintillator which determines how well the crystals are discriminated in an Anger-logic detector. Parallax effects are also studied by moving the point source radially out from the centre of the scanner to a distance of 10 cm. Our final goal is to investigate the contrast and noise characteristics of a lesion phantom for a high-Z LSO-based scanner and a medium-Z LaBr<sub>3</sub> scanner. We simulate small, hot and cold spheres in cylindrical phantoms. We use both a 20 × 70 cm cylinder to represent a thin patient, and a 27 × 70 cm cylinder to represent a larger, more typical patient (Surti *et al* 2003a, Kinahan *et al* 2004), and evaluate contrast and noise as function of imaging time. We analyse this while independently studying the importance of scatter and random coincidences as they affect the image properties. These simulations combine the effects of NEC and spatial resolution, but as yet the effects of pileup (spatial resolution and SF degradation) are not included in the image quality simulations.

## 2. Simulation tools

Described below are three Monte Carlo simulation tools that we have developed over the years for evaluation of PET system designs, and which have been used extensively in this investigation.

### 2.1. Montecrystal detector simulations (*Montecrystal*)

*Montecrystal* (Karp and Muehllehner 1985, Surti *et al* 2000) is a detector level simulation that starts with a  $\gamma$ -ray entering the detector at a pre-defined position and trajectory. The detector

is defined by the scintillator type and size, the lightguide design as well as varying PMT sizes and arrangements. Although many detector configurations can be simulated, here we model small discrete crystals with a continuous lightguide. The path and interactions of each  $\gamma$ -ray are traced using Compton scatter and photoelectric cross-sections as well as the Klein–Nishina equation, until it deposits all its energy or exits the detector. Scintillation photons are then generated at each interaction site based on the scintillator light yield. The path of each scintillation photon is traced until it gets absorbed or hits a PMT. This involves a detailed modelling of the crystal and lightguide surface boundaries as well as the reflector. The final outputs of the simulation are local energy spectra and position using a calculation based on Anger weighted centroid, as well as timing spectra for PMTs with a detailed model for the timing properties. In addition, various interaction probabilities for a scintillator material such as the photoelectric and photopeak efficiencies, as well as the number of misplaced events, can also be calculated. *Montecrystal* was used in the development of the  $\text{LaBr}_3$  detector design (Surti *et al* 2003b) just as it was done earlier with a GSO detector design (Surti *et al* 2000). Here it was also used as a component in the *HCRSim* and *EGS4*-based system simulations (see sections 2.2 and 2.3) for generating count-rate results and image quality phantom images.

## 2.2. High count-rate simulations (*HCRSim*)

The *HCRSim* Monte Carlo simulation was developed to accurately model pulse pileup behaviour in PET scanners based on Anger logic detectors (Mankoff *et al* 1989, Surti 2000) and to predict the behaviour of a scanner for a given phantom at varying count-rates. *HCRSim* models two coincident  $\gamma$ -rays (primary and secondary) from the phantom striking a pre-defined scanner subregion at a fixed position. The theoretical (no deadtime) singles and coincident count-rates for the entire scanner are calculated for a given activity level  $A$ , and single events are distributed spatially and temporally to model pulse pileup. Subsequent deadtime in the event triggering and integration is calculated, as well as event rejection based on a fixed energy gate. The electronic architecture assumed in *HCRSim* is based on the early PENN PET scanner (Muehllehner and Karp 1986), with localized trigger zones configured for a fixed number of PMTs and the width of light spread within the detector. Pulse pileup in the detector due to a spatial and temporal overlap of two unique interactions leads to a trigger deadtime as well as a rejection of coincident events due to energy gating. Additional deadtime from position calculation and processing electronics is not modelled here since these factors would be minimized in practice to match the requirements of the count-rate of the scanner. The energy gate rejection represents the intrinsic deadtime of the Anger-logic detector and is the major limitation on the count-rate performance of such scanners. The trigger and integrator deadtime represent the first level of electronics necessary for collecting all coincident events and help determine the complexity of the electronics architecture needed.

### 2.2.1. Input and set-up

- Singles, coincidence and correlated energy spectra from *EGS4* (see section 2.3) for a phantom in a pre-defined scanner and detector design.
- Singles and coincidence geometric efficiencies from *EGS4*.
- SF from *EGS4*.
- Point spread function (PSF) from *Montecrystal*.
- Single and coincidence interaction efficiencies from *EGS4*.
- Light response function (LRF) from *Montecrystal*.
- Scanner trigger arrangement, defined in *HCRSim*.

### 2.2.2. Output

- Singles, trues, scatter, randoms and NEC rates versus activity in the phantom.
- PSF as a function of count-rate (can be passed onto *EGS4*).
- Separation of trigger deadtime, energy gate rejection and event processing electronics deadtime in the scanner.

For this work, *HCRSim* was used to calculate true, scatter and random count-rates as a function of activity level in two different phantoms in a scanner design. From these, the subsequent NEC values are calculated (see figure 1). Additionally, we also used this simulation to calculate the change in SF and point spread function as a function of activity level due to pulse pileup and the use of a fixed energy gate (see figure 2).

### 2.3. EGS4 system simulations

An *EGS4*-based complete system simulation has been designed to simulate a cylindrical scanner with a given phantom placed inside the scanner field-of-view (Adam *et al* 1999). Besides modelling continuous and discrete crystal-based Anger-logic detectors, this simulation can also model septa of varying length and thickness placed inside the scanner for 2D imaging set-ups. Coincident photons are emitted within the phantom and their paths traced until they hit the scanner (photoelectric, Compton and Rayleigh scattering used since our energies are up to 662 keV). A stand alone routine from the *Montecrystal* simulation is used to trace the interactions within the detector but the scintillation photon tracing is not required as parametrized detector PSF (from *Montecrystal* and/or *HCRSim*) is used for position calculation at each interaction point. The output for this system simulation includes sinograms and/or list mode data with timing information for subsequent reconstruction with standard clinical software. The sinograms and list mode data are saved separately for total, trues, single scatter multiple scatter and septa scatter events. Additionally, energy spectra, efficiency information and SF as a function of energy gate are also calculated. For this investigation, we use this simulation to first investigate reconstructed spatial resolution as function of crystal size for different scintillators as well as degradation in reconstructed resolution due to pulse pileup at high count-rates. Finally, we evaluate two scanner designs and their impact on image quality by simulating hot and cold spheres in two cylindrical phantoms of different diameters representing two different size patients.

## 3. System design set-up

For all subsequent system design simulations, the scanner ring and patient port diameters were kept constant at 84 cm and 65 cm respectively. The annular lead shielding thickness was 2.5 cm. The detector was designed as a discrete crystal Anger-logic detector with the light spread restricted to a seven-PMT hexagonal cluster through an optimal lightguide design. The crystal packing fraction is 86% ( $4 \times 4 \text{ mm}^2$  crystal cross-section with a 4.3 mm crystal-to-crystal pitch). Table 2 gives a summary of other design parameters used in the simulations. The GSO scanner is similar to the current Philips Allegro scanner (Surti and Karp 2004) in its use of 20 mm long GSO crystals, number of PMTs, axial FOV and ring diameter. The LSO scanner design is just a substitution of GSO with similar size LSO crystals. For these simulations we ignored the radiation from  $^{176}\text{Lu}$  in LSO, and assumed that LSO and GSO had similar energy resolution. Since the stopping power and timing properties of LSO are better than GSO, the simulated LSO scanner will have higher sensitivity and count-rate performance than a GSO scanner given similar geometry and crystal size. The energy resolution for both GSO and LSO



**Table 2.** Scanner design parameters for simulations. The ELLD value defines the lower energy gate used in simulations.

	GSO	LSO	LaBr <sub>3</sub>
Axial FOV (cm)	18	18	25
Coincidence timing window (ns)	8	5	5
$\frac{\Delta E}{E}$ at 511 keV (%)	16	16	6.5
ELLD (keV)	420	420	470
Pixel length (mm)	20	20	30
PMT diameter (mm)	39	39	50, 39
Integration time (ns)	120	90	50

scanners was set at 16%, the value we measure with Allegro (Surti and Karp 2004) and the lower level energy gate (ELLD) was set at 420 keV. SF is defined here as  $\frac{Sc}{T+Sc}$ , where T and Sc are the true and scattered counts, respectively. The energy resolution of the LaBr<sub>3</sub> scanner was set at 6.5% which is a conservative choice compared to our recent laboratory measurements of about 5.5% with large LaBr<sub>3</sub> detector arrays (Kuhn *et al* 2004). Consequently, the ELLD value for the LaBr<sub>3</sub> scanner was set at 470 keV. For the LaBr<sub>3</sub> scanner we used a larger axial FOV (25 cm) and longer crystals (30 mm) because of the need to compensate for lower intrinsic sensitivity. In the future, a scanner based on LaBr<sub>3</sub> could afford to use longer crystals and a larger axial FOV because of the potential for lower scintillator cost compared to LSO. Additionally, we evaluate the LaBr<sub>3</sub> scanner with two PMT sizes; a 39 mm diameter PMT which is the size used in the GSO Allegro scanner and assumed for both the GSO and LSO scanner simulations, and a 50 mm diameter PMT since the very high light output of LaBr<sub>3</sub> enables one to achieve very good crystal discrimination with a larger PMT (Kuhn *et al* 2004). Also, there is a wider availability of 50 mm diameter PMTs with fast timing properties, thus making it easier to extend the design to a time-of-flight scanner. The position and energy calculation were performed using local seven-PMT cluster which contains most of the light from a given interaction (Surti *et al* 2000). The PMT trigger channels for the LSO, GSO and LaBr<sub>3</sub> (with 50 mm PMTs) scanner contained 12 PMTs each (3 PMTs in the transverse direction and 4 PMTs in the axial direction) with a one PMT overlap in the transverse direction and two PMT overlap in the axial direction between adjacent trigger channels. The LaBr<sub>3</sub> scanner using 39 mm PMTs had 15 PMTs per trigger channel (3 PMTs in the transverse direction and 5 PMTs in the axial direction), with the same one PMT overlap in the transverse direction and two PMT overlap in the axial direction between adjacent trigger channels.

Initially *EGS4* simulations were run to estimate the sensitivity and SF for two uniform cylinders of diameters 20 cm and 27 cm respectively, and a length of 70 cm. These results are shown in table 3. We have found that the 20 cm diameter phantom, the NEMA NU2-2001 standard (NEMA 2001), is representative of a thin patient, while the 27 cm diameter phantom better represents an average size patient more typically seen in the clinic (Surti *et al* 2003a, Kinahan *et al* 2004).

#### 4. NEC simulations

*HCRSim* calculations were performed for the three scanner designs with the two cylindrical phantoms. From the calculated count-rate the noise equivalent count (NEC) rate (Strother *et al* 1990) was derived. NEC is defined as

$$NEC = \frac{T \times T}{T + Sc + R} \quad (1)$$

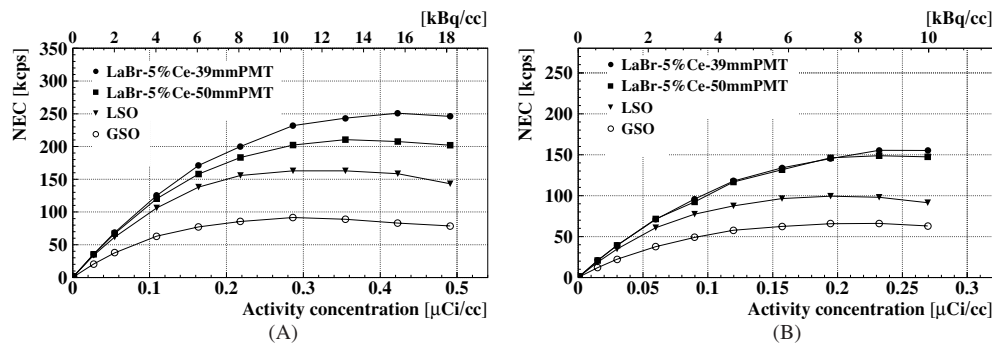


**Figure 1.** NEC rates calculated for different scanner designs for a 20 cm diameter (A) and 27 cm diameter (B) cylindrical phantom. Both cylinders were 70 cm long.

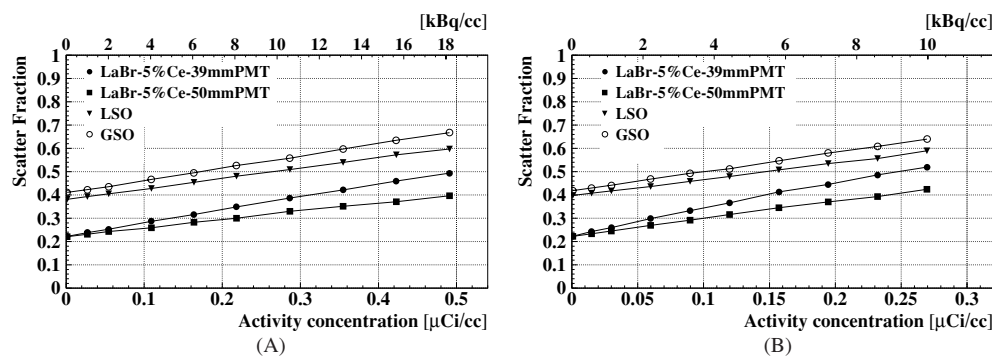


**Figure 2.** SF calculated for different scanner designs for a 20 cm diameter (A) and 27 cm diameter (B) cylindrical phantom. Both cylinders were 70 cm long.

**Table 3.** SF and sensitivity results for the three scanner designs studied here.

		GSO	LSO	LaBr <sub>3</sub>
20 cm × 70 cm cylinder	SF (%)	33	33	18
	Sensitivity (kcps/μCi/cc)	1300	1940	1660
27 cm × 70 cm cylinder	SF (%)	40	40	22
	Sensitivity (kcps/μCi/cc)	1470	2220	1840

where T, Sc and R are the true, scatter, and random coincidences over the object region (defined as 24 cm and 31 cm for the 20 cm and 27 cm diameter cylinders), and a smooth random subtraction is assumed. The calculated NEC plots are shown in figure 1. These results show that the LaBr<sub>3</sub> scanner with 39 mm PMTs produces the highest peak NEC rate and therefore can lead to improved signal-to-noise ratio (SNR) in the images. Despite lower sensitivity than LSO, LaBr<sub>3</sub> reaches a higher NEC due to reduced SF because of higher ELLD, reduced randoms-to-trues ratio because of longer axial FOV and reduced pileup at high activity levels. In the LSO and LaBr<sub>3</sub> scanners with 39 mm PMTs, the combined trigger plus integrator deadtime at the highest activity level is about 45% (at 0.49 μCi/cc) and 40% (at 0.27 μCi/cc) respectively for the 20 cm and 27 cm diameter cylinders. For the same two scanners, the



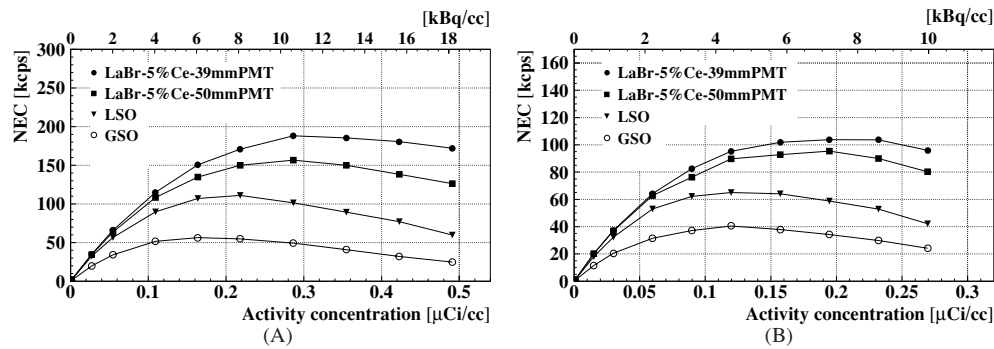


**Figure 3.** Effective NEC rates calculated for different scanner designs for a 20 cm diameter (A) and 27 cm diameter (B) cylindrical phantom after adjusting for change in SF as a function of count-rate due to the use of fixed energy gates. Both cylinders were 70 cm long.

deadtime due to energy gate rejection of coincident events is 55% for the 20 cm diameter cylinder. For the 27 cm diameter cylinder the energy gate rejection is 60% for LaBr<sub>3</sub> and 50% for LSO. Energy gate rejection is a physical limitation on the performance of these detectors and is determined by the PMT diameter and light spread within the detector, the scintillator decay time and the signal integration time. However, the trigger and integrator deadtime is an electronics limitation and could be reduced by faster integrators and smaller size trigger zones. Thus, with optimal triggering and integration schemes the NEC rates for the LSO and LaBr<sub>3</sub> scanners can be raised by as much as factor of 2.

An additional effect of pulse pileup when using a fixed energy gate is that the SF increases as a function of count-rate. At high rates, unrelated events overlap in spatial and temporal dimension leading to pulse pileup effects. As a result, some coincident events (true and scatter) which have energies within the fixed energy gate will, due to pulse pileup, be measured at higher energy values and thus get rejected. On the other hand, events which deposit energies below the ELLD value (more scatter than true events) may pileup and be measured with a higher energy, thus falling inside the accepted energy window. We studied this effect through our simulations for the different scanner designs and the two phantom sizes. SF as a function of activity concentration is plotted in figure 2. Figure 3 shows the effective NEC for the scanner designs after including the effect of SF variation as a function of count-rate. These results clearly show that there is an overall reduction in the effective NEC. The degradation in NEC due to pileup is therefore reduced by minimizing both the spatial and temporal overlap of events, both of which are achieved by using faster crystals and smaller PMTs. There is also a significant ( $\sim 20$ – $40\%$ ) decrease in the peak NEC rate depending on the scanner design when moving from the 20 cm diameter to 27 cm diameter cylinder. This is due to increased attenuation of the photons in a large object and increased scatter, which can be moderated by using a high ELLD as in the case of LaBr<sub>3</sub>. These results predict the significant degradation in image quality we expect to see when moving from a small to a large patient in the scanner.

## 5. Image resolution

### 5.1. Spatial resolution for $4 \times 4 \text{ mm}^2$ crystals size (low activity levels)

We also investigated the reconstructed image resolution for a point source placed in air for the LSO and LaBr<sub>3</sub> scanners with crystal cross section of  $4 \times 4 \text{ mm}^2$ . The crystal lengths of

**Table 4.** Reconstructed image resolution for a point source in air placed at the centre and 10 cm off-centre in different scanner designs. No background activity level was assumed here which could give rise to pulse pileup effects.

Crystal	FWHM (mm)	FWTM (mm)
At $r = 0$ cm		
LSO (39 mm PMT)	5.2	9.5
GSO (39 mm PMT)	5.7	10.3
LaBr <sub>3</sub> (39 mm PMT)	5.8	12.9
LaBr <sub>3</sub> (50 mm PMT)	5.9	13.0
At $r = 10$ cm		
LSO (39 mm PMT)	5.2	10.5
GSO (39 mm PMT)	5.7	11.5
LaBr <sub>3</sub> (39 mm PMT)	6.3	14.7
LaBr <sub>3</sub> (50 mm PMT)	6.6	15.0

20 mm for LSO and 30 mm for LaBr<sub>3</sub> were chosen because of the need to compensate for lower intrinsic sensitivity of LaBr<sub>3</sub>. For LaBr<sub>3</sub>, both 39 mm and 50 mm diameter PMTs were investigated. The simulations were performed with the point source placed at the centre as well as 10 cm off-centre positions in the scanner. The off-centre radial position is helpful in understanding the effect of parallax error on the image resolution. These simulations included effects due to Compton scatter within the scintillator as well as the impact on the detector point spread function due to scintillator light output and its collection by the PMTs. Images were reconstructed into 2 mm<sup>3</sup> voxels using the non-iterative 3D-FRP algorithm (Matej and Lewitt 2001) leading to a transverse image matrix size of 288 × 288 (for a 576 mm FOV) and 2 mm thick slices. The results are given in table 4. The full-width-at-half-maximum (FWHM) and full-width-at-tenth-maximum (FWTM) of the PSFs were determined in all three directions by forming one-dimensional (1D) response functions through the peak of the distribution in the three orthogonal directions. The width of these profiles at right angles to the direction of measurement is ~2 times the FWHM in those directions, rather than a single pixel, in order to reduce measurement variability. The FWHM and FWTM are calculated by linear interpolation between adjacent pixels at 1/2 or 1/10 of an estimate of the maximum value of the response function. This method of analysing spatial resolution is as prescribed in the NEMA NU2-2001 standards for clinical PET scanners (NEMA 2001). From this table, we see that the high-Z LSO has better spatial resolution compared to the medium-Z LaBr<sub>3</sub> and the relative difference is larger at the FWTM levels. Using larger PMTs (50 mm diameter) leads to a small difference in the image resolution of the LaBr<sub>3</sub> scanner due to a wider point spread function for the detector. At a radial distance of 10 cm, there is very little degradation in the LSO scanner image resolution, but a more significant degradation with LaBr<sub>3</sub> due to the use of longer crystals.

### 5.2. Spatial resolution for 4 × 4 mm<sup>2</sup> crystals size versus activity levels

In order to evaluate the impact on image resolution at high count-rates, an investigation of the degradation in image resolution of the scanners using 4 × 4 mm<sup>2</sup> crystals was performed as a function of activity within the FOV. Crystal lengths of 20 mm for GSO and LSO, and 30 mm for LaBr<sub>3</sub> were once again chosen based upon their use in whole-body scanner designs. *HCRSim* calculations were first performed to obtain the PSF as a function of activity level for a point source placed in uniform 20 cm diameter cylindrical phantoms (70 cm long). Again,

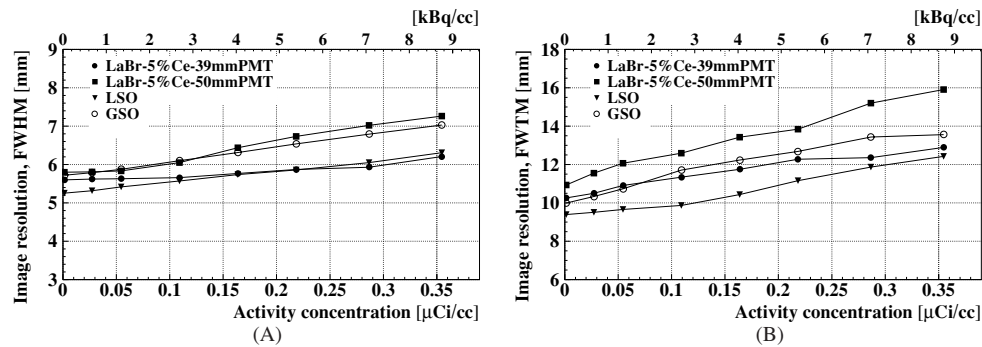


**Figure 4.** Reconstructed image resolution versus activity concentration for a point source in a 20 cm diameter by 70 cm long cylindrical phantom filled with water. Plot (A) is for the image FWHM while (B) shows the FWTM.

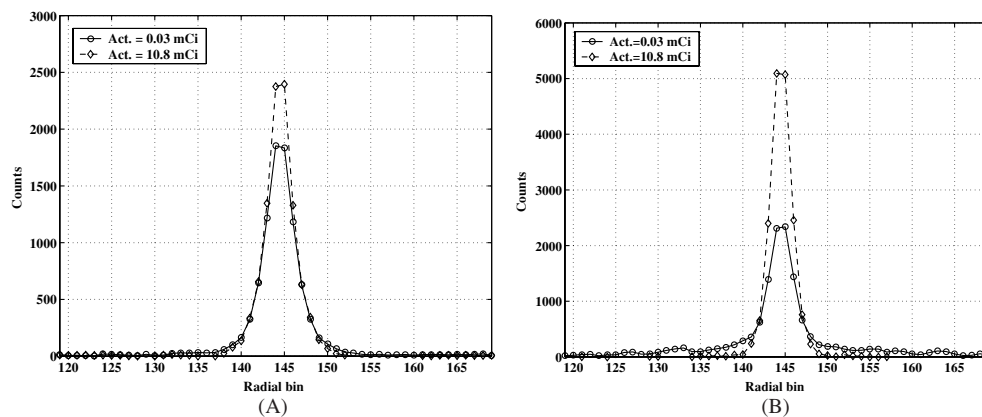


**Figure 5.** Image profiles used for calculating the spatial resolution values as shown in figure 4 for the LaBr<sub>3</sub> scanner with 39 mm PMTs (A) and the LSO scanner (B). The two activity levels are the lowest and highest activity concentrations investigated in figure 4. These figure profiles are for fixed number of simulated histories, and thus represent the counts collected for a fixed activity level inside the two scanners and same imaging times.

the images were reconstructed into  $2 \text{ mm}^3$  voxels using the non-iterative 3D-FRP algorithm (Matej and Lewitt 2001) leading to a transverse image matrix size of  $288 \times 288$  (for a 576 mm FOV) and 2 mm thick slices. The reconstructed image resolutions with the 20 cm cylinder are shown in figure 4. As the count-rate and pulse pileup increase in the scanner, LaBr<sub>3</sub> with 39 mm PMT has better spatial resolution. This is due to the reduced pulse pileup arising from the restriction of scintillation light to a seven-PMT cluster which is smaller in area for the 39 mm PMT compared to the 50 mm PMT. At high rates, the shorter decay time of 5% cerium LaBr<sub>3</sub> leads to reduced pileup effects relative to LSO, resulting in similar spatial resolution values for the two scintillators. Figure 5 shows a representative plot of a typical image profile used for calculating the spatial resolution values shown in figure 4. For clarity, we show only the case of the LaBr<sub>3</sub> with 39 mm PMTs and the LSO scanner (also with 39 mm PMTs). The two profiles are for the highest and lowest activity levels investigated and indicate the degradation in spatial resolution as shown earlier in figure 4. Note that the LSO profile is slightly narrower at low rates but the degradation at high rates is more significant

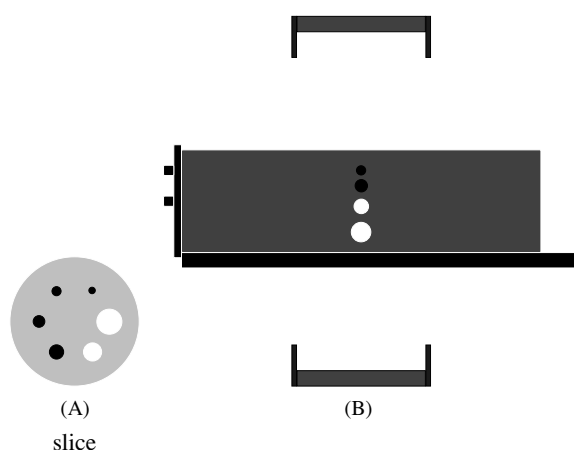


**Figure 6.** Transverse (A) and axial (B) views of the phantom in the scanner. The filled spheres are the four hot spheres with activity concentration of 8:1 with respect to background, while the open spheres are the large cold spheres.

than for LaBr<sub>3</sub>. It should be mentioned here that this degradation in spatial resolution as a function of activity level is dependent on pulse pileup effects in the scanner and its impact on the positioning algorithm used in determining the interaction position within the detector. Positioning algorithms other than the Anger logic algorithm we are using with a seven-PMT cluster could lead to differing behaviour and pulse pileup effects in the resulting reconstructed spatial resolution.

## 6. Image quality simulation results

Image quality simulations were performed using the *EGS4* code for the LSO and LaBr<sub>3</sub> scanner designs. The simulated phantoms were 20 cm diameter and 27 cm diameter (both 70 cm long) cylinders uniformly filled with water. Six spheres were simulated at the centre of the scanner at a radial distance of 5.72 cm for the cylinder centre. Figure 6 shows the phantom set-up for these simulations. The spheres, the uptake ratios and their radial arrangement are the same as in the NEMA NU2-2001 image quality phantom (NEMA 2001) but the simulation used a simple cylinder instead of a more anthropomorphic shape as prescribed by NEMA (23 cm × 30 cm cross-section similar to an average of 27 cm).

The two larger, water filled spheres (37 mm and 28 mm diameter) are cold, while the other six spheres (diameters of 28, 22, 17, 13 and 10 mm) had an activity concentration of 8:1 with respect to the background. The coincidence rates (randoms, trues and scatter) were taken to be at 0.32  $\mu\text{Ci/cc}$  and 0.18  $\mu\text{Ci/cc}$ , respectively for the 20 cm and 27 cm cylinders, close to the activity concentration values at which the NEC rates peak (see figure 1). The PSFs used were representative of the lowest activity levels without pulse pileup effects, and thus favour the intrinsic spatial resolution advantage of LSO over LaBr<sub>3</sub> (see figure 4). Also, a constant SF was assumed, although figure 2 shows that SF increases as a result of pulse pileup at high count-rates. Contrast recovery coefficients (CRC) were calculated using the NEMA NU2-2001 definition, however noise in the image was estimated by calculating the ratio of pixel standard deviation to its mean for a large central region drawn within a central slice of the reconstructed image. The simulations were performed for different count statistics, thereby representing varying imaging times. We analysed these images by normalizing the total amount

**Table 5.** Acquisition times and true, NEC and NEC for centre slice in the sinograms for the LaBr<sub>3</sub> and LSO scanners with 20 cm diameter and 27 cm diameter phantoms in the field-of-view. The counts are for the single bed position simulated here. The SF and RF are calculated over the region occupied by the object.

Total time for a 100 cm long scan (min)	Time for one frame (min)	Trues (Mcts)	NEC (Mcts)	NEC for centre slice (Mcts)
LaBr <sub>3</sub> scanner, 20 × 70 cm cylinder. SF = 17.1%, RF = 40.2%				
10.7	1.2	29.3	17.4	0.28
9.2	1.0	25.2	14.9	0.24
7.7	0.9	21.0	12.4	0.20
6.1	0.7	16.8	9.91	0.16
4.6	0.5	12.6	7.43	0.12
3.1	0.3	8.38	4.96	0.08
LaBr <sub>3</sub> scanner, 27 × 70 cm cylinder. SF = 21.4%, RF = 51.8%				
13.8	1.5	25.6	13.3	0.21
12.4	1.4	23.0	11.9	0.19
11.0	1.2	20.5	10.6	0.17
9.7	1.1	17.9	9.28	0.15
8.3	0.9	15.4	7.95	0.13
6.9	0.8	12.8	6.63	0.11
5.5	0.6	10.2	5.30	0.09
4.1	0.5	7.68	3.98	0.06
2.8	0.3	5.12	2.65	0.04
LSO scanner, 20 × 70 cm cylinder. SF = 27.8%, RF = 51.5%				
12.6	1.0	23.3	11.1	0.25
10.1	0.8	18.6	8.89	0.20
7.5	0.6	14.0	6.66	0.15
5.0	0.4	9.32	4.44	0.10
2.5	0.2	4.66	2.22	0.05
LSO scanner, 27 × 70 cm cylinder. SF = 35.1%, RF = 66.1%				
14.4	1.2	19.9	7.77	0.17
12.3	1.0	17.0	6.66	0.15
10.3	0.9	14.2	5.55	0.12
8.2	0.7	11.4	4.44	0.10
6.2	0.5	8.52	3.33	0.07
4.1	0.3	5.68	2.22	0.05
2.1	0.2	2.84	1.11	0.03

of emission time that will be needed to image a 100 cm long object with multiple bed positions (as prescribed by NEMA image quality measurement). For the short axial FOV scanner, a single bed position will therefore be of a shorter time duration than the long axial FOV scanner due to the increased number of bed positions (twelve instead of nine after assuming a 50% bed overlap) needed to cover the 100 cm of object being imaged. Image reconstruction was performed after a smooth random subtraction and a smooth scatter subtraction (based on the scatter only sinogram generated by the simulation). The scatter subtraction used here represents the ideal case where a perfect fit is achieved for the scatter data. Table 5 gives a summary of the true and NEC counts (for the one bed position simulated), and NEC for centre slice in the sinograms for the two scanner designs and the two image quality phantoms. In this table the random fraction, RF, is defined as  $\frac{R}{T+Sc}$ , where R, T and Sc are the random, true and scattered counts, respectively.

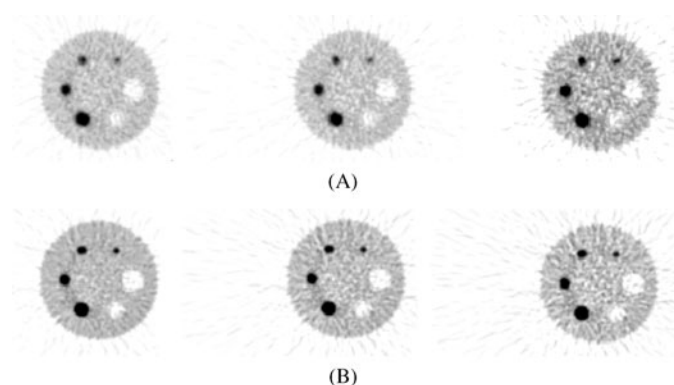


**Figure 7.** Central slice for the  $20 \times 70$  cm image quality phantom generated for three acquisition times in the LaBr<sub>3</sub> (A) and LSO (B) scanners after 3D-FRP reconstruction. The acquisition times, going from left to right, are 10.7, 7.7 and 4.6 min for the LaBr<sub>3</sub> scanner, and 12.6, 7.5 and 5.0 min for the LSO scanner.

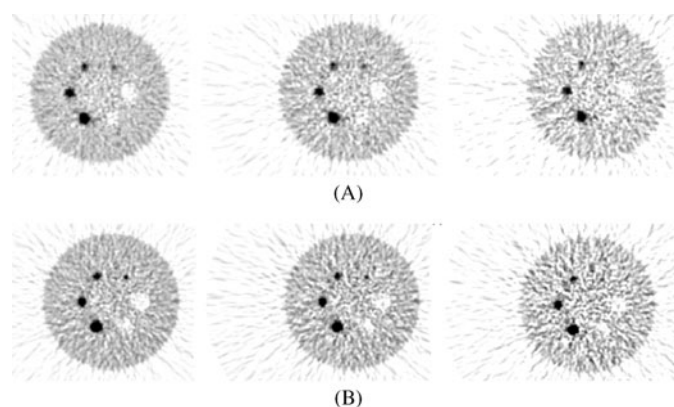


**Figure 8.** Central slice for the  $27 \times 70$  cm image quality phantom generated for three acquisition times in the LaBr<sub>3</sub> (A) and LSO (B) scanners after 3D-FRP reconstruction. The acquisition times, going from left to right, are 13.8, 8.3 and 4.1 min for the LaBr<sub>3</sub> scanner, and 14.4, 8.2 and 4.1 min for the LSO scanner.

Although the iterative 3D RAMLA (Browne and Pierro 1996, Daube-Witherspoon *et al* 2001) algorithm is normally applied to clinical data for Allegro, here we analysed the simulated data only with the non-iterative 3D-FRP (Matej and Lewitt 2001) algorithm, just as we did for the analysis of spatial resolution. This non-iterative reconstruction algorithm is considered to better illustrate the differences in scanner performance in terms of the statistical behaviour of the simulated data. Just as before for spatial resolution images, data were reconstructed into  $2 \text{ mm}^3$  voxels leading to a transverse image matrix size of  $288 \times 288$  (for a 576 mm FOV) and 2 mm thick slices. Figure 7 shows the central slice for three acquisition times for the  $20 \times 70$  cm cylinder in LaBr<sub>3</sub> (A) and LSO (B) scanners, respectively. The total acquisition times are 10.7, 7.7 and 4.6 min (left to right in figure 7(A)) for the LaBr<sub>3</sub> scanner, and 12.6, 7.5 and 5.0 min (left to right in figure 7(B)) for the LSO scanner. Note that these images represent a single realization of the simulated data and thus do not adequately reflect the uncertainty in the measurement. The short scan time data are included as part of the longer scan time data sets, and therefore are not statistically independent. Figure 8 shows the central slice for three



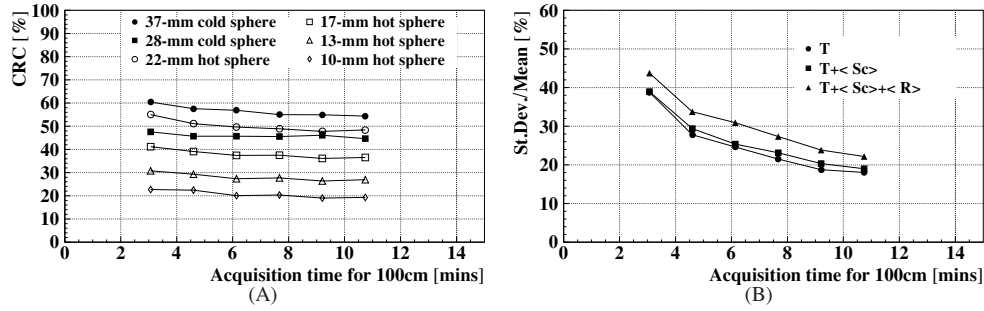


**Figure 9.** Contrast recovery (A) and noise (B) for the 20 × 70 cm image quality cylinder in the LaBr<sub>3</sub> scanner.

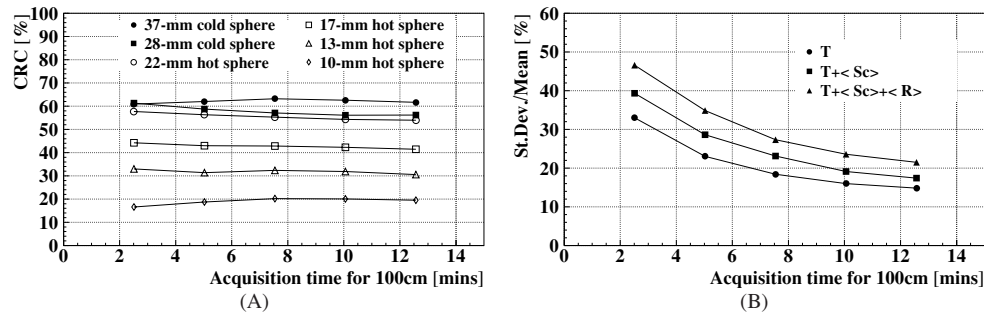


**Figure 10.** Contrast recovery (A) and noise (B) for the 20 × 70 cm image quality cylinder in the LSO scanner.

acquisition times for the 27 × 70 cm cylinder in LaBr<sub>3</sub> (A) and LSO (B) scanners, respectively. Here, the acquisition times are 13.8, 8.3 and 4.1 min (left to right in figure 8(A)) for the LaBr<sub>3</sub> scanner, and 14.4, 8.2 and 4.1 min (left to right in figure 8(B)) for the LSO scanner. The CRC and noise plots are shown in figures 9 and 10 respectively for the LaBr<sub>3</sub> and LSO scanner for the 20 × 70 cm cylinder. Similarly, the CRC and noise plots for the 27 × 70 cm cylinder are given in figures 11 and 12 respectively for the LaBr<sub>3</sub> and LSO scanners. The CRC values obtained with the LSO scanner are slightly better than those achieved in the LaBr<sub>3</sub> scanner due to the better spatial resolution of the detector at low count-rates without pulse pileup. On the other hand, the NEC and noise characteristics of a reconstructed transverse slice are slightly better for the LaBr<sub>3</sub> scanner, thereby showing the impact of reduced scatter and random coincidences in overcoming the reduced sensitivity of the LaBr<sub>3</sub> scanner. From the results for the 20 × 70 cm cylinder we conclude that it is possible to achieve good quality images after ~5 min of total emission scan time for a 100 cm long object. The results for the 27 × 70 cm cylinder, however, show that to achieve the same noise characteristics, a total scan time of more than 4–5 times that of the 20 cm cylinder is needed. However, it is still possible to achieve good image quality in less than 15 min.

From table 5, we see that the total collected NEC counts for the centre slice in the LSO scanner are about 10–15% less than that of the LaBr<sub>3</sub> scanner for a fixed total emission scan time (100 cm axial length), leading to a similar SNR (or noise, the inverse of SNR as defined here) which is proportional to the square root of NEC (Strother *et al* 1990). Our noise plots in figures 9 and 10 are in agreement with this conclusion.

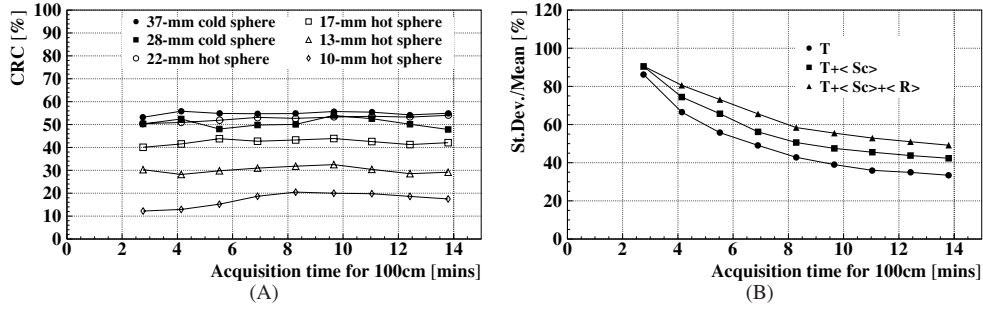


**Figure 11.** Contrast recovery (A) and noise (B) for the  $27 \times 70$  cm image quality cylinder in the LaBr<sub>3</sub> scanner.

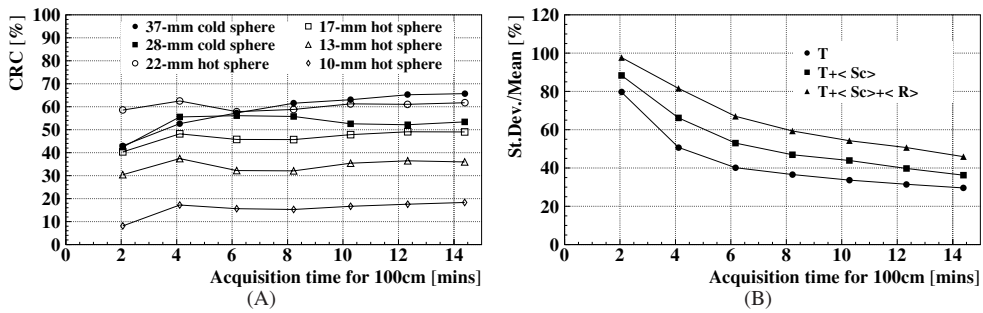


**Figure 12.** Contrast recovery (A) and noise (B) for the  $27 \times 70$  cm image quality cylinder in the LSO scanner.

As shown by Strother *et al* (1990), the SNR at the centre of a uniform cylinder is related to the NEC by

$$\text{SNR} = c \sqrt{\frac{4}{\pi}} \left( \frac{d}{D} \right)^{\frac{3}{2}} \left[ \frac{\text{avg}(a_c)}{a_c} \right]^{\frac{1}{2}} \times \sqrt{\text{NEC}} \quad (2)$$

where  $c$  is a constant,  $d$  is the image matrix size in one dimension,  $D$  is the cylinder diameter,  $a_c$  is the attenuation correction factor for the centre of the cylinder and  $\text{avg}(a_c)$  is the average attenuation correction factor. In comparing the expected SNR or noise in the images of a 20 cm and 27 cm cylinder, we need to include the effect of  $D$  as well as the attenuation which can be easily calculated. The value of  $\text{avg}(a_c)[a_c]$  is calculated to be 1.83 [6.67] and 2.24 [12.99] for the 20 cm and 27 cm diameter cylinders, respectively. The attenuation and object diameter terms in the SNR equation will then lead to a degradation by a factor of 2 in the noise characteristics of the 27 cm diameter cylinder when compared to the 20 cm cylinder for the same total acquisition time and scanner geometry. Together with the difference in the centre slice NEC values, we expect to see a total degradation by a factor of about 2.5 for both scanners when moving from the 20 cm cylinder to the 27 cm cylinder for a fixed acquisition time. From the noise plots, we verify that the noise degradation for both scanners is about 2.3 when moving from the 20 cm to the 27 cm cylinder.

## 7. Discussion and conclusions

In this investigation, we have shown that the medium-Z LaBr<sub>3</sub> scintillator can be used to design a 3D PET scanner with high performance measured in terms of sensitivity, NEC and spatial resolution. Using a scanner axial FOV of 25 cm and 30 mm long LaBr<sub>3</sub> crystals, we achieve ~85% sensitivity of an LSO scanner with 18 cm long axial FOV and 20 mm long crystals.

Better energy resolution of LaBr<sub>3</sub> allows the use of a higher ELLD setting in the LaBr<sub>3</sub> scanner as compared to an LSO scanner, leading to lower scatter fraction (SF) and random fraction (RF) values. For example, the SF values are 18% and 22% for the 20 cm and 27 cm diameter uniform cylinders (both 70 cm long) in the LaBr<sub>3</sub> scanner, while they increase to 33% and 40% respectively in the LSO scanner. LaBr<sub>3</sub> also has a shorter decay time than the LSO scintillator leading to reduced pulse pileup in the scanner. Our investigation shows that this leads to less degradation in SF (see figure 2) and spatial resolution (see figure 4) at high activity levels or count-rates. Together, the higher ELLD setting due to better energy resolution and shorter decay time lead to a higher peak NEC value for the LaBr<sub>3</sub> scanner despite having lower sensitivity than the LSO scanner. A reduction in pulse pileup, and hence a small increase in NEC can be achieved by reducing the PMT size from 50 mm to 39 mm diameter. Including the effect of SF degradation with count-rate leads to an effective NEC rate which, though reduced for all scanner configurations, is still higher for the LaBr<sub>3</sub> scanner.

Our image quality simulations combine effects of spatial resolution, scatter and random correction and scanner sensitivity. Due to its smaller Z, LaBr<sub>3</sub> has a lower photo-fraction which leads to increased crystal scatter and slightly worse spatial resolution with 4 mm cross-section crystals. This simulation does not include the effects due to pulse pileup which lead to a degradation of SF and spatial resolution, and which is less significant for LaBr<sub>3</sub> due to its faster decay. For the two scanner designs with LSO (18 cm axial FOV, 20 mm long crystals) and LaBr<sub>3</sub> (25 cm axial FOV, 30 mm long crystals), we evaluated image quality as a function of total emission scan time at an activity concentration near the peak NEC. The data were normalized to the total scan time for a 100 cm long axial scan with multiple bed positions and a 50% bed overlap. Our results for the two phantoms show that the contrast in a LaBr<sub>3</sub> scanner is a bit worse than the LSO scanner, while the noise improves slightly. Considering that these data are single realizations and include statistical uncertainties, we conclude that no significant differences are noticeable in the images acquired on the LSO and LaBr<sub>3</sub> scanners.

The significant increase in noise when moving from the 20 cm to 27 cm diameter cylinder indicates that poorer image quality will be achieved when imaging heavy patients. An increase by a factor of 2.5 in noise translates into an equivalent of more than six times the imaging time to achieve noise characteristics similar to that in slim patients. As shown in previous work (Surti and Karp 2004), incremental improvements could be achieved by further raising the ELLD level for individual scanners. More important is that the time-of-flight information will lead to a significant improvement in SNR due to variance reduction and/or contrast improvement. With high light output and fast timing characteristics, LaBr<sub>3</sub> (5% Ce) can provide timing resolution in the range of 300 ps for large Anger logic arrays in coincidence (Kuhn *et al* 2004, Surti *et al* 2003b). Similar measurements with a lutetium yttrium orthosilicate (LYSO, an LSO-like scintillator) detector array are around 600 ps. This aspect of the scanner development is being actively pursued in order to achieve additional improvements in image quality, especially in large patients.

Future investigations connected to this study will also involve folding the spatial resolution and SF degradation as a function of activity into the image quality simulations. This will help in investigating image quality as a function of count-rate, and also to understand further correlations with NEC. Also, since the *EGS4* simulations already have built-in

timing information, we intend to investigate the improvements expected in image quality with time-of-flight information using an iterative list-mode reconstruction algorithm. Since lesion detectability is a combination of the CRC and image noise, other more robust lesion detectability measures such as the matched non-prewhitening filter SNR (NPW-SNR) will also be used in evaluating these scanner designs.

## Acknowledgments

We would like to thank Dr Margaret Daube-Witherspoon and Matthew Werner of the University of Pennsylvania and Dr Klaus Fiedler of Philips Research Laboratories, Aachen, Germany for many useful discussions. This work was supported by DOE DE-FG02-88ER60642 and NIH R21-EB001684.

## References

- Adam L-E, Karp J S and Brix G 1999 Investigation of scattered radiation in 3D whole-body positron emission tomography using Monte Carlo simulations *Phys. Med. Biol.* **44** 2879–95
- Adam L-E, Karp J S, Daube-Witherspoon M E and Smith R J 2001 Performance of a whole-body PET scanner using curve-plate NaI(Tl) detectors *J. Nucl. Med.* **42** 1821–30
- Allemand R, Gresset C and Vacher J 1980 Potential advantages of a cesium fluoride scintillator for time-of-flight positron camera *J. Nucl. Med.* **21** 153–5
- Anger H O 1958 Scintillation camera *Rev. Sci. Instrum.* **29** 27–33
- Brix G, Zaers J, Adam L-E, Bellemann M E, Ostertag H, Trojan H, Haberkorn U, Doll J, Oberdorfer F and Lorenz W J 1997 Performance evaluation of a whole-body PET scanner using the NEMA protocol *J. Nucl. Med.* **38** 1614–23
- Browne J A and Pierro A R D 1996 A row-action alternative to the EM algorithm for maximizing likelihoods in emission tomography *IEEE Trans. Med. Imaging* **15** 687–99
- Casey M E and Nutt R 1986 A multicrystal two dimensional BGO detector system for positron emission tomography *IEEE Trans. Nucl. Sci.* **33** 460–5
- Daube-Witherspoon M E, Matej S, Karp J S and Lewitt R M 2001 Application of the row action maximum likelihood algorithm with spherical basis functions to clinical PET imaging *IEEE Trans. Nucl. Sci.* **48** 24–30
- Erdi Y, Nehmeh S, Mulnix T, Humm J and Watson C 2004 PET performance measurements for an LSO-based combined PET/CT scanner using the NEMA NU2-2001 standard *J. Nucl. Med.* **45** 813–21
- Karp J and Muehllehner G 1985 Performance of a position sensitive scintillation detector *Phys. Med. Biol.* **30** 643–55
- Karp J S, Surti S, Freifelder R, Daube-Witherspoon M E, Cardi C, Adam L-E and Muehllehner G 2003 Performance of a GSO PET camera *J. Nucl. Med.* **44** 1340–9
- Kinahan P, Surti S, Badawi R, Fakhri G E, Karp J and Lewellen T 2004 Effect of patient thickness on noise equivalent count rate for 2D and fully-3D whole-body PET imaging *J. Nucl. Med.* **45** (Suppl) 102
- Kuhn A, Surti S, Karp J, Raby P, Shah K, Perkins A and Muehllehner G 2004 Design of a lanthanum bromide detector for TOF PET *Trans. Nucl. Sci.* **51** at press
- Lewellen T K, Kohlmyer S G, Miyaoka R S, Kaplan M S, Stearns C W and Schubert S F 1996 Investigation of the performance of the general electric ADVANCE positron emission tomograph in 3D mode *IEEE Trans. Nucl. Sci.* **43** 2199–206
- Mankoff D A, Muehllehner G and Karp J S 1989 The high countrate performance of a two-dimensionally position-sensitive detector for positron emission tomography *Phys. Med. Biol.* **34** 437–56
- Matej S and Lewitt R M 2001 Direct fourier reconstruction with fourier reprojection for fully 3-D PET *IEEE Trans. Nucl. Sci.* **48** 1378–85
- Moses W and Derenzo S 1999 Prospects for time-of-flight PET using LSO scintillator *IEEE Trans. Nucl. Sci.* **46** 474–8
- Moszyński M, Kapusta M, Wolski D, Szawlowski M and Klamra W 1998 Energy resolution of scintillation detectors: readout with large area avalanche photodiodes and photomultipliers *IEEE Trans. Nucl. Sci.* **45** 472–7
- Muehllehner G and Karp J 1986 A positron camera using position-sensitive detectors: PENN-PET *J. Nucl. Med.* **27** 90–8
- Mullani N A, Ficke D C, Hartz R, Markham J and Wong W H 1981 System design of a fast PET scanner utilizing time-of-flight *IEEE Trans. Nucl. Sci.* **28** 104–7

- Nellemann P, Hines H, Braymer W, Muehllehner G and Geagan M 1995 Performance characteristics of a dual head SPECT scanner with PET capability *IEEE MIC Conference Record* number 3 pp 1751–5
- NEMA 2001 *NEMA Standards Publication NU 2-2001* (Rosslyn, VA: NEMA)
- Perkins A E, Muehllehner G, Surti S and Karp J S 2003 Performance measurements of a pixelated NaI(Tl) PET scanner *IEEE Trans. Nucl. Sci.* **50** 373–7
- Shah K et al 2002 LaBr<sub>3</sub>:ce scintillators for gamma ray spectroscopy *IEEE MIC Conference Record* pp N8–2
- Strother S C, Casey M E and Hoffmann E J 1990 Measuring PET scanner sensitivity: relating countrates to image signal-to-noise ratios using noise equivalent counts *IEEE Trans. Nucl. Sci.* **37** 783–8
- Surti S 2000 A model of scintillation detector performance for positron emission tomography *PhD Thesis* University of Pennsylvania
- Surti S, Badawi R, Holdsworth C, Fakhri G E, Kinahan P and Karp J 2003a A multi-scanner evaluation of PET image quality using phantom studies *IEEE Nucl. Sci. Symp. and Med. Imaging Conf. (Portland, OR, 19–25 October 2003)*
- Surti S and Karp J 2004 Imaging characteristics of a 3-dimensional gso whole body PET camera *J. Nucl. Med.* **45** 1040–9
- Surti S, Karp J S, Freifelder R and Liu F 2000 Optimizing the performance of a PET detector using discrete GSO crystals on a continuous lightguide *IEEE Trans. Nucl. Sci.* **47** 1030–6
- Surti S, Karp J S, Muehllehner G and Raby P S 2003b Investigation of lanthanum scintillators for 3-D PET *IEEE Trans. Nucl. Sci.* **50** 348–54
- Surti S, Karp J, Perkins A, Freifelder R and Muehllehner G 2003c Design evaluation of A-PET: a high sensitivity animal PET camera *IEEE Trans. Nucl. Sci.* **50** 1357–63
- Ter-Pogossian M M, Mullani N A and Ficke D S 1981 Photon time-of-flight assisted positron emission tomograph *J. Comput. Assist. Tomogr.* **5** 227–39
- Uribe J, Li H B H, Yokoyama S, Zhang N, Wang J, Dobbs F R and Wong W-H 1999 Basic imaging performance characteristics of a variable field of view PET camera using quadrant sharing detector design *IEEE Trans. Nucl. Sci.* **46** 491–7
- van Eijk C W E 2002 Inorganic scintillators in medical imaging *Phys. Med. Biol.* **47** R85–106
- van Loef E P P D, van Eijk C, Kramer K and Gudel H 2001 High-energy-resolution scintillator: Ce<sup>3+</sup> activated LaBr<sub>3</sub> *Appl. Phys. Lett.* **79** 1573–5
- Wienhard K et al 2002 The ECAT HRRT: performance and first clinical application of the new high resolution research tomograph *IEEE Trans. Nucl. Sci.* **49** 104–10
- Wong W, Uribe J, Hicks K and Hu G 1995 An analog decoding BGO block detector using circular photomultipliers *IEEE Trans. Nucl. Sci.* **42** 1095–101